The Journal of Experimental Biology 211, 267-273
Published by The Company of Biologists 2008
doi:10.1242/jeb.006155

Research article

Vortex-wake interactions of a flapping foil that models animal swimming and flight

David Lentink[1,*], Florian T. Muijres[1,2], Frits J. Donker-Duyvis[2] and Johan L. van Leeuwen[1]

[1]Department of Experimental Zoology, Wageningen University, 6709 PG Wageningen, The Netherlands and [2]Faculty of Aerospace Engineering, Delft University of Technology, 2600 GB Delft, The Netherlands

*Author for correspondence (e-mail: david.lentink@wur.nl)

Accepted 15 October 2007

Summary

The fluid dynamics of many swimming and flying animals involves the generation and shedding of vortices into the wake. Here we studied the dynamics of similar vortices shed by a simple two-dimensional flapping foil in a soap-film tunnel. The flapping foil models an animal wing, fin or tail in forward locomotion. The vortical flow induced by the foil is correlated to (the resulting) thickness variations in the soap film. We visualized these thickness variations through light diffraction and recorded it with a digital high speed camera. This set-up enabled us to study the influence of foil kinematics on vortex-wake interactions. We varied the dimensionless wavelength of the foil (λ^*=4–24) at a constant dimensionless flapping amplitude (A^*=1.5) and geometric angle of attack amplitude ($A_{\alpha,geo}$=15°). The corresponding Reynolds number was of the order of 1000. Such values are relevant for animal swimming and flight.

We found that a significant leading edge vortex (LEV) was generated by the foil at low dimensionless wavelengths (λ^*<10). The LEV separated from the foil for all dimensionless wavelengths. The relative time (compared with the flapping period) that the unstable LEV stayed above the flapping foil increased for decreasing dimensionless wavelengths. As the dimensionless wavelength decreased, the wake dynamics evolved from a wavy von Kármán-like vortex wake shed along the sinusoidal path of the foil into a wake densely packed with large interacting vortices. We found that strongly interacting vortices could change the wake topology abruptly. This occured when vortices were close enough to merge or tear each other apart. Our experiments show that relatively small changes in the kinematics of a flapping foil can alter the topology of the vortex wake drastically.

Key words: flapping foil, vortex dynamics, vortex-wake interaction, swimming, flight, soap tunnel.

Introduction

The complex fluid mechanics of many animals that swim or fly is governed by the non-linear formation, shedding and dynamics of vortices (e.g. Dickinson et al., 2000). These vortices can potentially affect performance through their interactions with wings, fins or tails (e.g. Birch and Dickinson, 2003). The nature of the interactions is related to the kinematics of the wing, fin or tail, though the precise relationship is not yet known. This relationship is better understood for vibrating cylinders. Williamson and Roshko (Williamson and Roshko, 1988) reported in their inspirational paper how the vortex-wake topology of a vibrating cylinder depends on both the dimensionless amplitude, (A^*, Eqn 2) and the dimensionless wavelength (λ^*, Eqn 1), which is analogous to the dimensionless stride length and the inverse of the reduced frequency. Williamson and Roshko showed that synchronization (lock-in) can occur between the driving frequency of a vibrating cylinder and multiples (n) of the natural von Kármán (eigen-) frequency of the vortical flow. Synchronization resulted in periodic vortex wakes shed by the vibrating cylinder. The synchronization region consists of two bands of periodic wakes; in between, the wake is mostly aperiodic. Both synchronization bands are approximately elliptic in the parametric space spanned by A^* and λ^*: $A^*=\frac{1}{4}\sqrt{n\cdot\lambda_0^{*}-\lambda^{*2}}$, in which λ_0^* is the dimensionless wavelength based on the von Kármán frequency [independently found by Lentink (Lentink, 2003) and Ponta and Aref (Ponta and Aref, 2005)]. The first band is related to the von Kármán frequency itself ($\lambda_0^*\approx5$; A^*=0), the second to a third of that frequency ($\lambda_0^*\approx15$; A^*=0) (Note λ_0 is proportional to the inverse of frequency). Similar computational fluid dynamic studies of two-dimensional plunging foils (Lewin and Haj-Hariri, 2003; Lentink and Gerritsma, 2003) showed that the wake and fluid forces that act on a foil can be either periodic or aperiodic. Lentink and Gerritsma (Lentink and Gerritsma, 2003) found evidence for the existence of chaotic modes. The actual mode depends on the dimensionless wavelength and amplitude of the foil. The simulations showed that the near-wake dynamics (wake mode) of the foil directly affect the character of the fluid forces (periodic *versus* aperiodic) that act on the foil. Hence these results suggest that kinematics potentially have a significant influence on the periodicity of the wake of a flapping foil and its corresponding propulsive and lifting forces.

Here we studied the possible significance of vortex dynamics as a physical constraint to animal locomotion in fluids. A two-dimensional flapping foil is a simplified model of animal wings, fins or tails. We aimed to visualize and quantify the vortex-wake interactions of such a two-dimensional flapping foil as a function of its kinematics. To this end we decided to flap our foil in a soap-film tunnel: a thin layer of water between two molecular layers of soap molecules, driven by gravity (Rutgers et al., 2001). Gharib and Derango (Gharib and Derango, 1989) have demonstrated that a soap tunnel is effective for studying a wide range of two-dimensional flow phenomena. To our knowledge

Couder et al. (Couder et al., 1989) were the first to actively drive an object similar to a flapping foil in a soap film. In their pioneering work they studied the vortical flow generated by a vibrating cylinder that moved through a static soap film. As far as we are aware, the present study is the first to consider a flapping foil in a soap tunnel.

Earlier flapping foil studies have demonstrated both the value and effectiveness of a two-dimensional approach for gaining new insight into animal locomotion (Triantafyllou et al., 1993; Dickinson, 1994; Wang, 2000a; Wang, 2000b; Miller and Peskin, 2004). We foresee, nevertheless, that a full study of vortex dynamics as a physical constraint to animal locomotion would require an extension to three dimensions. In three dimensions the vortex dynamic complexity is further increased (e.g. Buchholz and Smits, 2006; von Ellenrieder et al., 2003) by processes such as vortex stretching (Guyon et al., 2001). High Reynolds numbers also facilitate three-dimensional instabilities that can result, for example, in coherent vortices with a turbulent structure (e.g. Van Dyke, 1982). Note, however, that two-dimensional vortex dynamic mechanisms are a sub-set of three-dimensional vortex dynamics. This makes two-dimensional flapping foil studies intrinsically valuable for our understanding of how vortices generated by animals that swim or fly interact with each other and the animal.

Here we focused on the two-dimensional dynamics of vortices shed by a flapping foil in forward motion as a function of dimensionless wavelength. This enabled us to gain more insight into the generation and dynamics of leading-edge vortices (LEVs) and vortex-wake interactions.

Materials and methods

Parameterization of the flapping foil

Similar to others (Triantafyllou et al., 1993; Dickinson, 1994; Wang, 2000a; Wang, 2000b; Miller and Peskin, 2004), we modelled the kinematics of wings, fins and tails with a two-dimensional sine-shaped excursion and rotation of the foil with a phase difference of 90°. The five main scaling variables of such a foil are: (1) the flapping frequency f of the excursion and rotation, which are equal to the animal's flapping frequency; (2) the excursion amplitude A, typically taken at the radius of gyration or 75% of an animal's wing, fin or tail semi-span; (3) the geometric angle of attack amplitude $A_{\alpha,\mathrm{geo}}$, taken at the same span-wise position as the excursion amplitude A; (4) the (average) forward speed of the foil U_∞, which is equivalent to the animal's forward speed; and (5) the chord length of the foil l, which represents the average chord length of an animal wing, fin or tail (we will describe foil shape in the next section).

Non-dimensionalization allowed us to objectively quantify the scale effects (Guyon et al., 2001) of a flapping foil. We followed an approach described in Lentink and Gerritsma (Lentink and Gerritsma, 2003) that is consistent from hovering fight, with zero dimensionless wavelength, to fast forward flight, for which the dimensionless wavelength approaches infinity. The resulting non-dimensionalization is defined below and illustrated in Fig. 1. The dimensionless wavelength (λ*) represents the number of foil lengths travelled forward during one stroke:

$$\lambda^* = \frac{U_\infty}{fl}, \tag{1}$$

in which U_∞ is the free-stream velocity, f the flapping frequency and l the foil length. The non-dimensional amplitude A^* represents the amplitude of the foil excursion A with respect to the foil length l:

$$A^* = \frac{A}{l}. \tag{2}$$

The amplitude-based Strouhal number St_A is equal to the ratio of dimensionless amplitude (A^*) and dimensionless wavelength (λ*) and scales with the maximum induced angle of attack at mid-stroke (see Fig. 1 and Eqn 4):

$$St_A = \frac{A^*}{\lambda^*}. \tag{3}$$

The effective angle of attack amplitude $A_{\alpha,\mathrm{eff}}$ is equal to the angle of attack amplitude induced by the flapping foil minus the geometric angle of attack amplitude $A_{\alpha,\mathrm{geo}}$:

$$A_{\alpha,\mathrm{eff}} = \arctan(2\pi \cdot St_A) - A_{\alpha,\mathrm{geo}}. \tag{4}$$

The time-averaged velocity U_{ave} of the flapping foil can be approximated as follows (Lentink and Gerritsma, 2003):

$$U_{\mathrm{ave}} \approx \sqrt{U_\infty^2 + (4Af)^2}. \tag{5}$$

Based on this average velocity we define the time-averaged Reynolds number Re, which represents the relative importance of inertia *versus* viscosity:

$$Re = Re_\infty \sqrt{1 + (4\mathrm{St}_A)^2}, \tag{6}$$

in which:

$$Re_\infty = \frac{U_\infty l}{\nu}, \tag{7}$$

where ν is the kinematic viscosity. In our model we chose the dimensionless wavelength (λ*) and amplitude ratio (A^*) as independent variables following Williamson and Roshko (Williamson and Roshko, 1988), to which we needed to add the angle of attack amplitude. The other parameters (St_A and Re) can therefore be expressed as a function of λ*, A^* and Re_∞ (Eqns 3–6).

Foil shape and flapping mechanism

The foil is a flat plate and its kinematics is generated with a crankshaft mechanism. The foil has a thickness t of 0.3 mm and

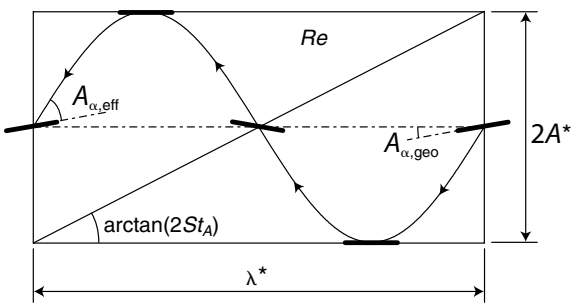

Fig. 1. A graphical representation of the non-dimensional parameters of a sinusoidally flapping foil: dimensionless wavelength λ*, amplitude ratio A^*, amplitude-based Strouhal number St_A, geometric angle of attack amplitude $A_{\alpha,\mathrm{geo}}$, effective angle of attack amplitude $A_{\alpha,\mathrm{eff}}$, and stroke-averaged Reynolds number Re.

length l of 3 mm; hence it has a relative thickness of 10%. It is made out of a thin piano-steel wire bent into an 'L' shape. The horizontal part of the L functions as the foil in the soap film while the vertical part is mounted to the mechanism. The foil is mounted such that its axis of rotation is located at approximately 1/4 foil length (with respect to the leading edge). The leading edge of the foil is naturally rounded as a result of bending the wire, while the trailing edge is more or less blunt (flat) as a result of cutting the wire.

Our custom-built flapping mechanism is illustrated and described in Fig. 2. It consists of a crankshaft that generates both the stroke amplitude and a 90° out-of-phase angle of attack amplitude. The stroke amplitude is reduced with a pantograph and the angle of attack amplitude is reduced with a series of pulleys. A crankshaft mechanism cannot generate pure sinusoidal stroke amplitudes (Fig. 3). The angle of attack amplitude is, however, very close to being sinusoidal. In our experiments we applied $A_{\alpha,geo}$=15°. All deviations from purely sinusoidal kinematics are therefore as follows: the root mean square (r.m.s.) deviation of the excursion is 9.4% of A^*, and the r.m.s. deviation of $A_{\alpha,geo}$ is 0.4%. Note that the resulting stroke kinematics is not fully symmetric (Fig. 3).

Soap-film tunnel set-up

The present soap-film tunnel design (Fig. 4) is based on a gravity-driven, constant flow design by Rutgers et al. (Rutgers et al., 2001). The ratio of the soap-film width to thickness is of the order of 10 000 (Rutgers et al., 2001). The vortices generated in a soap film are therefore roughly 1000 times wider than they are thick, indicating that the flow field is essentially two-dimensional. As a result, a soap film is ideally suited for studying the two-dimensional vortical field behind a flapping foil. The corresponding vorticity field is directly correlated to minute thickness variations in the soap film (Chomaz and Costa, 1998; Rivera et al., 1998; Chomaz, 2001). These thickness variations can be visualized as they diffract light transmitted by a monochromatic lamp (Rutgers et al., 2001). We used a high-frequency, low pressure, SOX lamp (Philips) as light source. The resulting diffraction patterns were recorded time-resolved with a Redlake® (Redlake MotionPro, San Diego, CA, USA) high-speed camera system at 800 frames s^{-1} and a shutter time of 1/1600 s. This visualization and capturing technique enabled us to time-resolve the dynamics of the vorticity field effectively: little experimental and computational time is required for generating and interpreting the flow field of a soap tunnel in order to study complex vortex dynamic flows as a function of foil kinematics. Additionally, the flow visualizations have a certain artistic appeal.

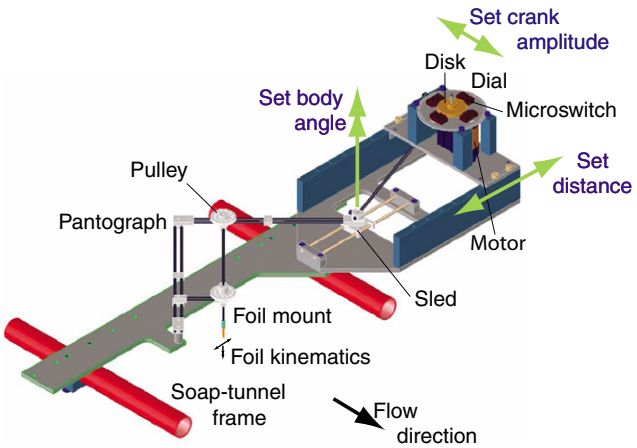

Fig. 2. Flapping mechanism as mounted on the soap-tunnel framework (further illustrated in Fig. 4). The flapping mechanism consists of a crank mechanism that generates a stroke and angle of attack amplitude that are 90° out of phase with respect to each other. The angle of attack amplitude is reduced with a series of pulleys. The stroke amplitude is reduced with the aid of a pantograph. The flapper is driven by a DC motor. We mounted a special dial-plate with one microswitch (four are drawn) on the motor housing. This switch is pressed by a disk with a small knob in a phase we predetermined with the dial; in this way the camera can be triggered in a specific phase of the stroke. The angle of attack and stroke amplitude can be varied independently by changing the distance between the motor and the sled, indicated by 'set distance', and the arm length of the crankshaft ('set crank amplitude'), which is hidden under the motor house in its current position. Finally, the angle of the stroke plane of the foil can be set with respect to the free-stream direction by rotating the whole crank mechanism, which is indicated by 'set body angle'; in this study it is zero (as drawn).

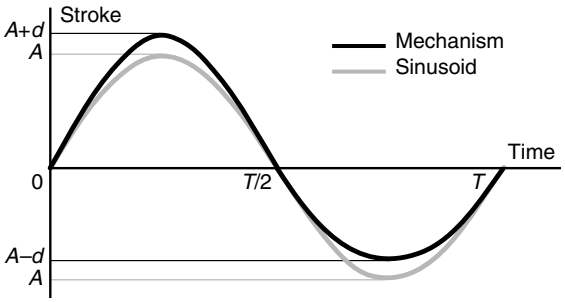

Fig. 3. Stroke kinematics generated with our flapping mechanism. The stroke kinematics deviates with magnitude +/–d from a sine with amplitude A.

The most important physical variables of the soap film in our experimental set-up are its flow velocity, U_∞, and kinematic viscosity, ν. The viscosity of a soap film is not exactly known. However, accurate measurements by Martin and Wu (Martin and Wu, 1995) show that the viscosity, for a solution similar to ours, is approximately 1×10^{-6} m^2 s^{-1} (4% Dawn dishwashing detergent). We adopted this value for our solution of approximately 2% Dawn dishwashing detergent (Procter & Gamble, professional line). The soap-film velocity varies over the width of the film from zero at the walls (due to the no-slip condition) to maximum velocity in the middle. In air the resulting velocity profile obtained in a soap tunnel corresponds to a plug-like profile (Rutgers et al., 2001). We determined the variation of the flow velocity over the amplitude range of the flapping foil with particle-tracking velocimetry (PTV) of small pollutants in the soap film. The flow velocity was determined at three locations; at the start, middle and end of the stroke, of which the maximum standard deviation was 12%. The accuracy of the frequency measurement was better than 3% while the length of the foil was measured with an accuracy of approximately 5%.

Applied foil kinematics and soap-tunnel settings

We chose to study the influence of dimensionless wavelength on vortex-wake interactions inspired by a two-dimensional numerical study of insect flight (Lentink and Gerritsma, 2003). In this study of a plunging foil, a chaotic mode was found for λ^*=4 at Re=150. Similar simulations for λ^*=6 (Lentink, 2003) revealed a periodic mode. A plunging foil is, however, a limited model of insect flight and animal locomotion in general – the main reason being that thrust generation is minimal for zero geometric angle of attack

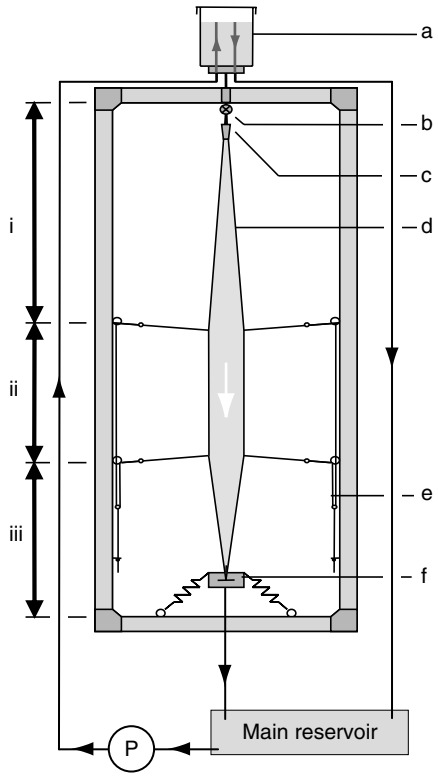

Fig. 4. The soap-film tunnel is mounted in an inclined frame and driven by gravity. It consists of three sections: a divergent section (i), the constant width (60 mm) test section in which the foil flaps (ii) and a convergent section (iii). The soap reservoir (a) produces a constant head by using an overflow. The soap flows from the reservoir (a) through a tuning valve (b) and an oval nozzle made out of a plastic pipette (c). At the pipette (c) the soap film starts: it runs down, driven by gravity, between two 1 mm thick Nylon wires (d) into tunnel sections (i–iii). The Nylon wires are pulled apart with 0.2 mm Dynema fishing lines (e). Finally the soap is collected in a reservoir (f) and is drained into the main soap reservoir and pumped (P) back again to the top reservoir (a).

amplitude. This is due to a minimal frontal surface area for the pressure difference to act on in the forward direction (Lentink and Gerritsma, 2003). Therefore, we chose to fix the angle of attack amplitude in this study to a more realistic value, $A_{\alpha,geo}$=15°. This value facilitates the generation of significant thrust (note that the corresponding time-averaged lift is approximately zero if the near flow field is symmetric). The stroke amplitude of the foil was adopted from the numerical study; A^*=1.5. Such amplitude has relevance for insects and bird wings and fish fins and tails, but is not related to a specific animal (because time time-averaged lift is approximately zero, the present study relates best to forward swimming and climbing flight, e.g. during vertical take-off). Intrigued by the numerically found dependence of wake mode on dimensionless wavelength, we decided to study the wake patterns and the LEV as a function of dimensionless wavelength for $4 \leqslant \lambda^* \leqslant 24$. We fixed the soap-film speed to approximately U_∞=0.20 m s^{-1}. As a result, the time-averaged Reynolds number ranged between 600 and 900, the lowest obtainable range in our facility. These Reynolds numbers were 4–6 times higher than in the numerical study (Lentink and Gerritsma, 2003; Lentink, 2003).

Results

We have visualized and subsequently classified the vortical wakes of our flapping foil as a function of dimensionless wavelength inspired by the nomenclature developed by Williamson and Roshko (Williamson and Roshko, 1988) for vibrating cylinders. In this approach, the number of single vortices (S) and vortex pairs (P) are identified per stroke (period). However, such a classification is almost never fully objective. The shedding of tiny vortices, which usually merge immediately with larger vortices, can make the flow analysis tedious. Williamson and Roshko, for example, had to work around the coalescence of many small and large vortices in some cases. This approach is nevertheless suitable for describing and sorting out the relationship between the shedding of leading- and trailing-edge vortices (LEVs and TEVs) and the subsequent formation of the wake as a function of dimensionless wavelength.

For all experiments we started at zero flapping frequency, which we subsequently increased monotonically to obtain the desired dimensionless wavelength. In this way we avoided hysteresis loops. Similar to earlier findings for hovering insect flight (Dickinson, 1994), we found that the LEV is unstable at all dimensionless wavelengths in two dimensions. We defined a LEV as unstable when it moved from the leading edge towards the trailing edge during the stroke. We restricted ourselves to scoring whether the LEV was generated and whether its centre passed the trailing edge before stroke reversal. If a LEV did not pass the trailing edge we refer to it as 'attached'. We further described the wake structure as a function of vortices shed at the leading and trailing edge of the foil. We loosely refer to a 'bifurcation' when the wake switches between two seemingly co-existing wake patterns at a constant wavelength [an introduction to bifurcations can be found in Addison (Addison, 1997)]. We found an array of wake patterns and vortex interactions, which we will illustrate starting at λ^*=24 and ending at λ^*=4.

Vortex wake for λ^*=12–24

The effective angle of attack amplitude was low at these high dimensionless wavelengths, A_α=7°–23°, hence no LEVs or TEVs were formed during a stroke (Fig. 5A). Although a minute LEV started to become visible at λ^*=12, it remained negligible compared with the ones found for lower dimensionless wavelengths. The basic wake pattern emerged from a wake instability that resulted in the roll-up of the shear layer behind the foil into an alternating row of vortices. This wake shed along the sinusoidal path of the flapping foil is similar to the von Kármán vortex street shed by a cylinder; hence our name wavy von Kármán wake: WK. The Reynolds number was close to 600 and the specific parameters in Fig. 5A are: λ^*=24, A^*=1.5, A_α=7° and Re=600.

Vortex wake for λ^*=8.6–10

At these dimensionless wavelengths, A_α ranged from 29° to 33° and as a result LEVs and TEVs were generated, which formed in most cases a pair when shed (Fig. 5B). Due to the high dimensionless wavelengths, however, the initial vortices were shed long before the end of the stroke, enabling the flow to generate and shed a secondary LEV and/or TEV within the same stroke. During the upstroke two LEVs and two TEVs were formed, which formed two vortex pairs (2P), in contrast to the downstroke when one LEV and two TEVs were generated, which formed a single vortex (S) and a vortex pair (P). The net result was a 3P+S vortex wake that evolved out of the vortices (3LEVs+4TEVs) shed during a flap period. At λ^*=8.6 a bifurcation was observed: the vortex wake switched between the current 3P+S and a 2P+2S mode (Fig. 6, bifurcation 1). LEVs were in all cases shed before the end of the stroke. The

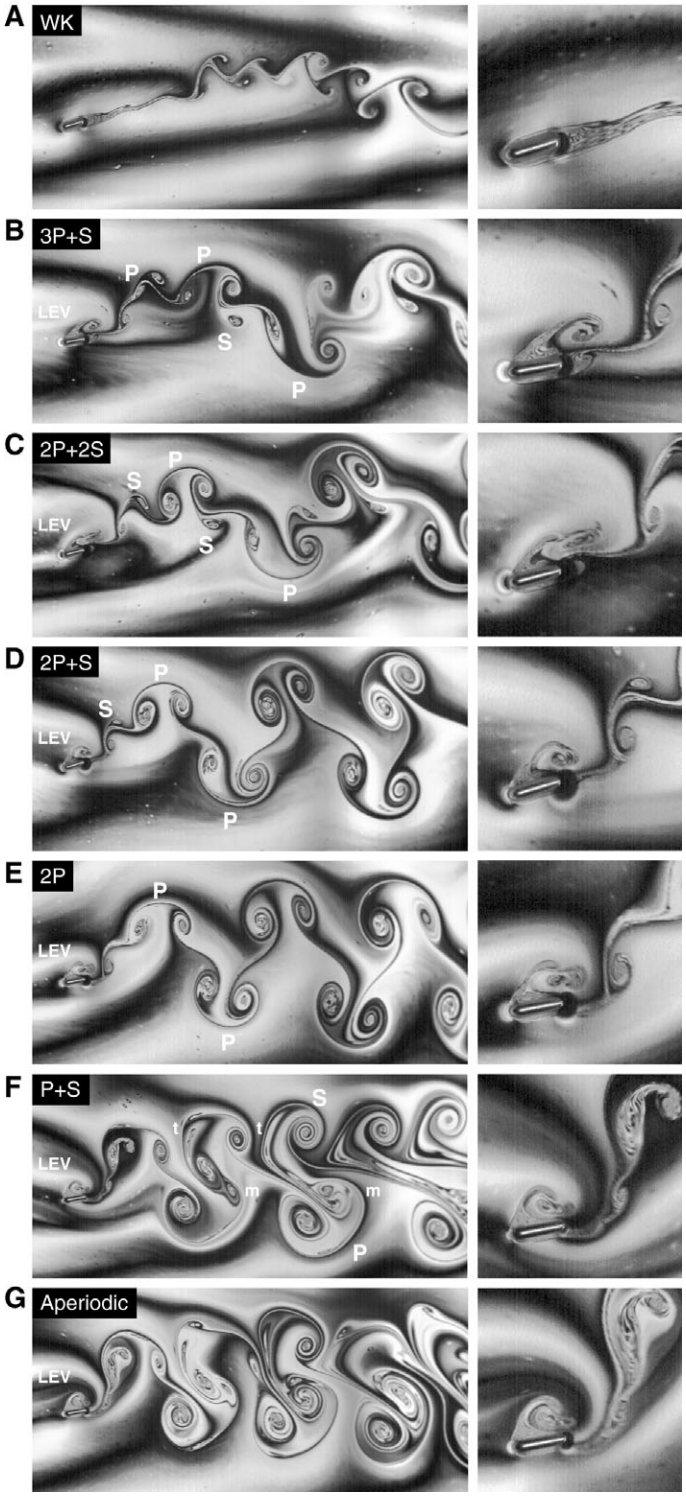

Fig. 5. Visualization of the evolution of vortex-wake topology and the attachment of the LEV for decreasing dimensionless wavelength λ*. The wake dynamics evolves from a wavy von Kármán wake (WK) into an aperiodic wake densely packed with large interacting vortices (A–G, left: overview wake, right, zoomed in on LEV). The soap film flows from left to right and all images have been taken mid-stroke during the downstroke. The leading edge vortex is indicated by LEV, a vortex pair by P, a single vortex by S, vortex tearing by t, and vortex merging by m. Note that the naming of the wakes is simplified and should be taken as a guideline: we have neglected a few tiny vortices that are shed at some advanced ratios for simplicity. (Note: A, λ*=24; B, λ*=10; C, λ*=7.9; D, λ*=6.8; E, λ*=6.3; F, λ*=4.5; G, λ*=4.0.)

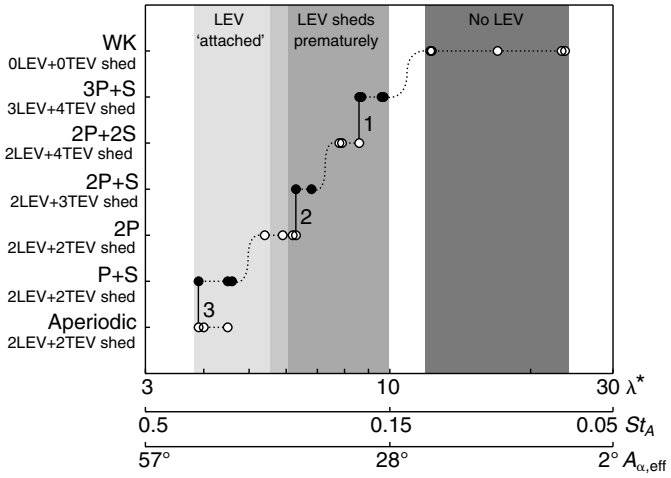

Fig. 6. Summary of vortex-wake topologies, the attachment of the LEV and the number of shed LEVs and TEVs as a function of dimensionless wavelength λ*. Note that the effective angle of attack amplitude A_α strongly increases with decreasing λ*, which in part explains the increasing vortex size. The more densely packed wake at low λ* is a direct result of the smaller distances between the shed vortices. Solid lines (1–3) indicate bifurcations found in one movie sequence. Filled and open circles are for easy distinction between modes only.

Reynolds number for this range of λ* was again close to 600 while the parameters of Fig. 5B are: λ*=10, A^*=1.5, A_α=29° and Re=600.

Vortex wake for λ*=6.8–8.6

For these dimensionless wavelengths A_α ranged from 33° to 39°, and the vortices became increasingly larger due to the higher effective angle of attack (Fig. 5C). We find that one LEV and two TEVs were formed and shed during both the up- and downstroke. These vortices (2LEV+4TEV) organized into a 2P+2S wake. For lower dimensionless wavelengths, the wake evolved from a 2P+2S into a 2P+S mode. The dimensionless wavelengths at which this happened have, however, not been determined. LEVs were in all cases shed before the end of the stroke. The Reynolds number range was 600–700 while the parameters resulting in Fig. 5C are: λ*=7.9, A^*=1.5, A_α=29° and Re=600.

Vortex wake for λ*=6.3–6.8

The effective angle of attack amplitude started at 39° and ended at 41° for this range of λ* (Fig. 5D). During the upstroke one LEV and two TEVs were shed, which formed a P+S. During the downstroke one LEV and one TEV were shed, which formed a P. The final result was a 2P+S wake pattern. LEVs were again shed before stroke reversal. The single vortex was subsequently merged with a vortex pair downstream. We observed a bifurcation between the 2P+S and 2P modes at λ*=6.3 (Fig. 6, bifurcation 2). The Reynolds number for this range of λ* was close to 700 while the parameters of Fig. 5D are: λ*=6.8, A^*=1.5, A_α=39° and Re=700.

Vortex wake for λ*=5.4–6.3

The effective angle of attack amplitude ranged from 41° to 45° in this case (Fig. 5E). During each flapping period two LEVs and two TEVs were shed, which evolved into a 2P wake pattern. At these low dimensionless wavelengths the LEVs and TEVs stayed attached to the wing long enough to prevent the development of secondary vortices during a stroke. We did not identify a bifurcation between the current and the next mode found at lower

dimensionless wavelengths. The LEVs stayed attached to the wing until stroke reversal, while the Reynolds number ranged from 700 to 800. The parameters that resulted in Fig. 5E are: λ^*=6.3, A^*=1.5, A_α=41° and Re=700.

Vortex wake for λ^*=3.9–4.6

As A_α further decreased from 49° to 53° we encounted the strongest vortex-wake interactions (Fig. 5F,G). At the beginning of the downstroke, the LEV created during the upstroke was still attached to the foil. This LEV interacted with the newly developing TEV and finally these vortices either merged or were torn apart when they came within critical distance. This merging m and tearing t had a significant influence on the wake formation and resulted in a strongly asymmetric P+S wake mode. In the same wake some tiny vortices were shed that either merged or were torn apart due to mutual interactions. The parameters of Fig. 5F are λ^*=4.5, A^*=1.5, A_α=49° and Re=800.

Within this range of dimensionless wavelengths we found two co-existing wake modes that were sensitive to small disturbances, resulting in bifurcations (Fig. 6, bifurcation 3). The second wake mode was an aperiodic variant of the first, which is illustrated in Fig. 5G (λ^*=4.0, A^*=1.5, A_α=52° and Re=900). The overlap of the two modes is probably due to a combination of experimental challenges, as they occurred at the highest frequencies obtainable, and dynamical complexity. The LEV was 'attached' for all these dimensionless wavelengths, while the Reynolds number ranged from 800 to 900.

Discussion

The 'attachment' of the LEV, the number of shed LEVs and TEVs, and the resulting wake patterns and bifurcations of the flapping foil as a function of dimensionless wavelength are summarized in Fig. 6.

Attachment of the LEV

The two-dimensional LEVs generated by our flapping foil were unstable at all dimensionless wavelengths. The LEVs grew stronger due to the higher effective angle of attack amplitudes at low λ^*. For such λ^* we define the LEV as 'attached' because its centre has not yet travelled past the trailing edge at stroke reversal (Fig. 6). 'Attachment' of LEVs at low λ^* is beneficial for both lift and thrust generation because the low pressure core of the LEV can act on the wing during the full stroke (Dickinson, 1994; Ellington et al., 1996). Note that the position of such LEVs is stable with respect to the leading edge in three-dimensional models of hovering insects due to three-dimensional flow effects such as span-wise flow (Ellington et al., 1996; Lentink and Dickinson, 2005).

Vortex-wake formation and interactions

Our experimental analysis shows that the wake topology depends in part on the number of LEVs and TEVs shed in the wake (Fig. 6). The vortex modes were found to bifurcate between subsequent modes in three instances. These bifurcations influenced only small (single) vortices at high dimensionless wavelengths (Fig. 6, bifurcations 1 and 2). Hence we consider these bifurcations to be weak. At low dimensionless wavelengths it involved, however, vortex merging and tearing, which altered the vortex-wake topology drastically (Fig. 6, bifurcation 3). We consider such bifurcations and the corresponding vortex interactions to be strong. Compared with weak bifurcations, strong bifurcations appeared more sensitive to disturbances and the wake modes switched more abruptly.

The number of shed vortices (LEVs and TEVs) decreased with dimensionless wavelength because they had relatively less time to develop and shed from the foil. At very low dimensionless wavelengths, the barely shed LEVs will be hit by the foil during stroke reversal, resulting in strong foil–vortex interactions. The similarly strong vortex merging (Cerretelli and Williamson, 2003; Leweke et al., 2001) and tearing interactions depend critically on the timing of vortex shedding, because it determines the spacing of the vortices in the wake.

Asymmetric and aperiodic vortex wakes

We expect that both wake asymmetry and wake aperiodicity could be relevant to animal locomotion. The wakes presented here resulted from slightly asymmetric stroke kinematics. This makes it difficult to rigorously determine the influence of vortex interactions on the asymmetry of a wake. Numerical studies (e.g. Lewin and Haj-Hariri, 2003; Lentink and Gerritsma, 2003) convincingly show, however, that asymmetric wakes can arise from symmetric foil kinematics. The orientation of the asymmetric wakes (e.g. in Fig. 5F; with respect to the horizontal axis) depends on the start-up condition and is sensitive to large disturbances. For λ^*=3.9–4.6 we found strong vortex-wake interactions that resulted in an aperiodic mode. This corresponds with the chaotic mode found numerically for a roughly similar plunging foil by Lentink and Gerritsma (Lentink and Gerritsma, 2003). Using the current set-up we were, however, unable to determine whether the aperiodic mode is chaotic (Addison, 1997).

Vortex-wake synchronization?

We found almost exclusively periodic vortex wakes in this study. We did not find a (confined) synchronization 'band' for our flapping foil similar to those found for cylinders (Williamson and Roshko, 1988). We think this could be due to two reasons: first, the number of experiments that we were able to perform with our set-up in the parameter space of the flapping foil (λ^*, A^*, $A_{\alpha,\mathrm{geo}}$) was smaller; and second, such 'bands', or regions, might well be very complex in shape for a flapping foil, because a translating (non-flapping) foil has a range of natural vortex-shedding frequencies as a function of angle of attack (α) (e.g. Katz, 1981; Dickinson and Götz, 1993) instead of a single shedding frequency (like cylinders have). We conclude that the role of vortex-wake synchronization in the wake of a flapping foil remains to be determined, in both two dimensions and three dimensions, for a wide range of flapping kinematic parameters and more realistic wing, fin and tail morphologies.

Finally, we observed in our two-dimensional experimental set-up that relatively small changes in the kinematics of a flapping foil can alter the topology of its vortex wake drastically. Numerical simulations have shown that the corresponding fluid mechanic forces can change drastically too (e.g. Lewin and Haj-Hariri, 2003; Lentink and Gerritsma, 2003). The possible relevance of similar vortex-wake bifurcations for animals that swim or fly could be studied, inside and outside of the behavioural envelope of the animal, with realistic three-dimensional robotic animal models (e.g. Ellington et al., 1996). We hypothesize that such a study might provide new insight into the influence of vortex-wake dynamics on the swimming and flight behaviour of animals.

List of abbreviations and symbols

λ^*	dimensionless wavelength
λ_0^*	dimensionless wavelength based on von Kármán frequency
A	flapping amplitude

A^*	dimensionless flapping amplitude
$A_{\alpha,\mathrm{eff}}$	effective angle of attack amplitude
$A_{\alpha,\mathrm{geo}}$	geometric angle of attack amplitude
d	amplitude deviation from sinusoidal kinematics
f	flapping frequency
l	foil length
n	multiple (of the natural von Kármán frequency)
Re	time-averaged Reynolds number of a flapping foil
Re_∞	Reynolds number of a flapping foil based on U_∞
St_A	amplitude-based Strouhal number
t	thickness of foil
U_{ave}	time-averaged velocity of the flapping foil
U_∞	forward velocity of the flapping foil; equivalent to free-stream velocity

We would like to thank Jos van den Boogaard for helping us with the construction and design of the soap tunnel, Maarten Rutgers for advice and good soap, Bas van Oudheusden for co-supervising F.T.M. at the TU Delft, and the Delft Aerospace Engineering workshop for building the flapping mechanism. Finally we would like to thank Andrew Biewener, Geoff Spedding and Ulrike Müller for valuable comments.

References

Addison, P. S. (1997). *Fractals and Chaos: An Illustrated Course*. Bristol: Institute of Physics Publishing.

Birch, J. M. and Dickinson, M. H. (2003). The influence of wing-wake interactions on the production of aerodynamic forces in flapping flight. *J. Exp. Biol.* **206**, 2257-2272.

Buchholz, J. and Smits, A. J. (2006). On the evolution of the wake structure produced by a low aspect ratio pitching panel. *J. Fluid Mech.* **546**, 433-443.

Cerretelli, C. and Williamson, C. H. K. (2003). The physical mechanism for vortex merging. *J. Fluid Mech.* **475**, 41-77.

Chomaz, J. M. (2001). The dynamics of a viscous soap film with soluble surfactant. *J. Fluid Mech.* **442**, 387-409.

Chomaz, J. M. and Costa, M. (1998). Thin film dynamics. In *Free Surface Flows* (*CISM Courses and Lectures 391*) (ed. H. C. Kuhlmann and H. J. Rath), pp. 44-99. New York: Springer.

Couder, Y., Chomaz, J. M. and Rabaud, M. (1989). On the hydrodynamics of soap films. *Physica D* **37**, 384-405.

Dickinson, M. H. (1994). The effects of wing rotation on unsteady aerodynamic performance at low Reynolds numbers. *J. Exp. Biol.* **192**, 179-206.

Dickinson, M. H. and Götz, K. G. (1993). Unsteady aerodynamic performance of model wings at low Reynolds numbers. *J. Exp. Biol.* **174**, 45-64.

Dickinson, M. H., Farley, C. T., Full, R. J., Koehl, M. A. R., Kran, R. and Lehman, S. (2000). How animals move: an integrative view. *Science* **288**, 100-106.

Ellington, C. P., Van den Berg, C., Willmott, A. P. and Thomas, A. L. R. (1996). Leading-edge vortices in insect flight. *Nature* **384**, 626-630.

Gharib, M. and Derango. P. (1989). A liquid film (soap film) tunnel to study two-dimensional laminar and turbulent flows. *Physica D* **37**, 406-416.

Guyon, E., Hulin, J. P., Petit, L. and Mitescu, C. D. (2001). *Physical Hydrodynamics*. Oxford: Oxford University Press.

Katz, J. (1981). A discrete vortex method for non-steady separated flow over an airfoil. *J. Fluid Mech.* **102**, 315-328.

Lentink, D. (2003). Influence of airfoil shape on performance in insect flight. MSc thesis, Delft University of Technology, The Netherlands.

Lentink, D. and Dickinson, M. H. (2005). Structure, stability and strength of leading edge vortices in insect flight. *Comp. Biochem. Physiol.* **141A**, S139.

Lentink, D. and Gerritsma, M. I. (2003). Influence of airfoil shape on performance in insect flight. AIAA Paper AIAA-2003-3447, www.aiaa.org.

Leweke, T., Meunier, P., Laporte, F. and Darracq, D. (2001). Controlled interaction of co-rotating vortices. Proceedings of the 3rd ONERA-DLR Aerospace Symposium, ODAS.

Lewin, G. C. and Haj-Hariri, H. (2003). Modelling thrust generation of a two-dimensional heaving airfoil in a viscous flow. *J. Fluid Mech.* **492**, 339-362.

Martin, B. and Wu, X. L. (1995). Shear flow in a two-dimensional couette cell: a technique for measuring the viscosity of free-standing liquid films. *Rev. Sci. Instrum.* **66**, 5603-5608.

Miller, L. A. and Peskin, C. S. (2004). When vortices stick: an aerodynamic transition in tiny insect flight. *J. Exp. Biol.* **207**, 3073-3088.

Ponta, F. L. and Aref, H. (2005). Vortex synchronization regions in shedding from an oscillating cylinder. *Phys. Fluids* **17**, 011703.

Rivera, M., Vorobieff, P. and Ecke, R. E. (1998). Turbulence in flowing soap films: velocity, vorticity, and thickness fields. *Phys. Rev. Lett.* **81**, 1417-1420.

Rutgers, M. A., Wu, X. L. and Daniel, W. B. (2001). Conducting fluid dynamics experiments with vertically falling soap films. *Rev. Sci. Instrum.* **72**, 3025-3037.

Triantafyllou, G. S., Triantafyllou, M. S. and Grosenbaugh, M. A. (1993). Optimal thrust development in oscillating foils with application to fish propulsion. *J. Fluids Struct.* **7**, 205-224.

Van Dyke, M. (1982). *An Album of Fluid Motion*. Stanford: The Parabolic Press.

von Ellenrieder, K. D., Parker, K. and Soria, J. (2003). Flow structures behind a heaving and pitching finite-span wing. *J. Fluid Mech.* **490**, 129-138.

Wang, Z. J. (2000a). Two dimensional mechanism for insect hovering. *Phys. Rev. Lett.* **85**, 2216-2218.

Wang, Z. J. (2000b). Shedding and frequency selection in flapping flight. *J. Fluid Mech.* **410**, 323-341.

Williamson, C. H. K. and Roshko, A. (1988). Vortex formation in the wake of an oscillating cylinder. *J. Fluids Struct.* **2**, 355-381.